

Supplementary Information

Electrochemically Induced Metal- vs. Ligand-Based Redox Changes in Mackinawite: Identification of a Fe³⁺ and Polysulfide-Containing Intermediate

Sebastian A. Sanden, Robert K. Szilagyi, Yamei Li, Norio Kitadai, Samuel M. Webb, Takaaki Yano, Ryuhei Nakamura, Masahiko Hara, Shawn E. McGlynn

Contents:

1. Sulfur K-edge X-Ray Absorption Near Edge Spectroscopy of $n(\text{Fe}^{2+}\text{S}^{2-})_{(s)}$	2
2. Peak-fitted Raman spectra of electrochemically treated $n(\text{Fe}^{2+}\text{S}^{2-})_{(s)}$	3
3. Calculated Raman spectra of [2Fe2S] rhombs.....	5
4. Calculated Raman spectra of FeS nanoparticles	11
5. Calculated Raman spectra of FeS complexes.....	16
6. Literature References	25

The experimental data including Raman spectra, S K-edge XANES data, cyclic voltammograms, and results of DFT calculations for molecules, complexes, and nanoparticles can be accessed at DOI: 10.5281/zenodo.5056738 or <https://zenodo.org/record/5056738> .

1. Sulfur K-edge X-Ray Absorption Near Edge Spectroscopy of $n(\text{Fe}^{2+}\text{S}^{2-})_{(\text{s})}$

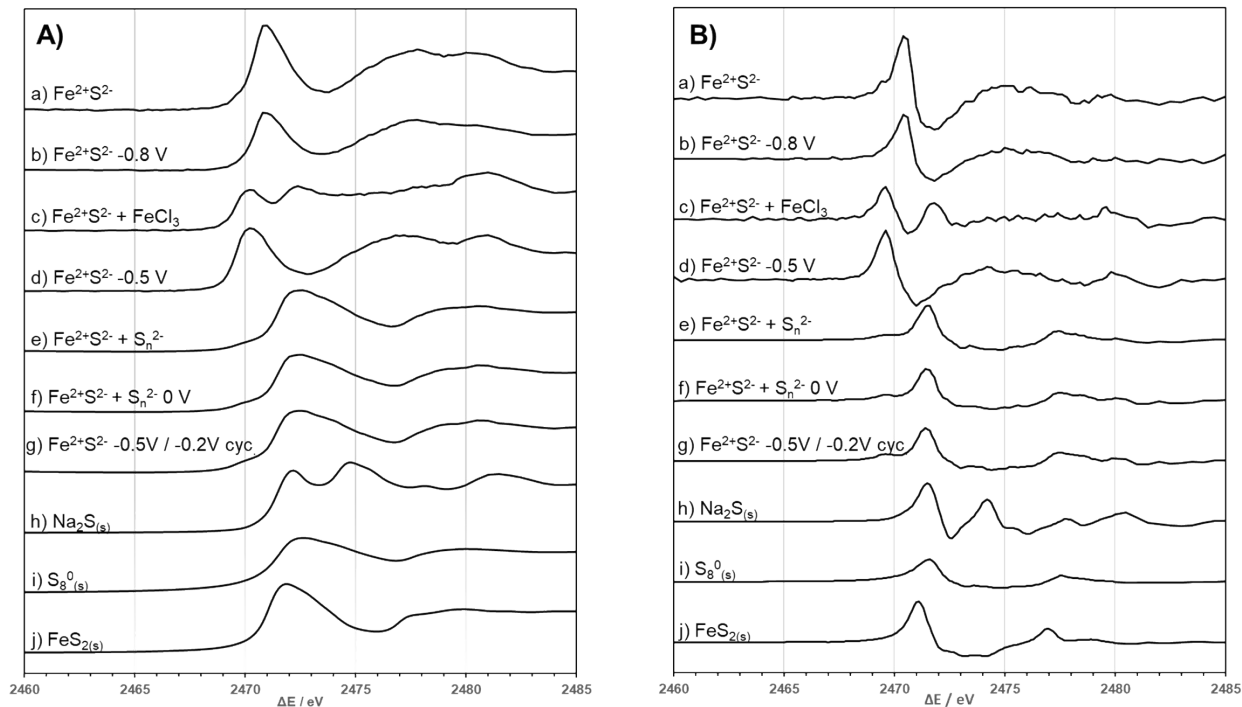


Figure S1, Normalized sulfur K-edge X-ray near-edge absorbance spectra of electrochemically treated $n(\text{Fe}^{2+}\text{S}^{2-})_{(\text{s})}$ samples and reference compounds (**A**) and their respective first derivative spectra obtained from the software ATHENA (**B**). The spectra in Panel A correspond to a) freshly precipitated $n(\text{Fe}^{2+}\text{S}^{2-})_{(\text{s})}$, b) electrochemically reduced $n(\text{Fe}^{2+}\text{S}^{2-})_{(\text{s})}$ at -0.8 V vs. AgCl, c) reference material obtained by the addition of 1 mM $\text{FeCl}_3(\text{aq})$ to 400 μM $n(\text{Fe}^{2+}\text{S}^{2-})_{(\text{s})}$, d) $n(\text{Fe}^{2+}\text{S}^{2-})_{(\text{s})}$ at a potential of 0.8 V for 1.5 h and -0.5 V for 2 h, e) $n(\text{Fe}^{2+}\text{S}^{2-})_{(\text{s})}$ to which 1 mM $\text{Na}_2\text{S}_n^{2-}(\text{aq})$ was added, f) 400 μM $n(\text{Fe}^{2+}\text{S}^{2-})_{(\text{s})}$ with 1 mM $\text{Na}_2\text{S}_n^{2-}(\text{aq})$ at a potential of 0 V for 10 min, and g). $n(\text{Fe}^{2+}\text{S}^{2-})_{(\text{s})}$ to which a cyclic potential from -0.5 V to -0.2 V was applied for 3.5 h with a scanning speed of 10 mV/s. Spectra of reference compounds of sodium sulfide (Sigma-Aldrich), 99.99% elemental sulfur and acid-washed pyrite (obtained from Strem Chemicals) are shown by traces h) to j), respectively. The energy scale was calibrated by setting the first XANES pre-edge feature maximum of sodium thiosulfate to 2472.02 eV.

2. Raman spectroscopy of electrochemically treated $n(\text{Fe}^{2+}\text{S}^{2-})_{(\text{s})}$

The peak positions of Raman spectra of freshly precipitated $n(\text{Fe}^{2+}\text{S}^{2-})_{(\text{s})}$, then dried samples after exposure to different applied electrode potentials were determined by peak fitting using OriginPro 2020b (OriginLabs). The baseline of $n(\text{Fe}^{2+}\text{S}^{2-})_{(\text{s})}$ spectra at -0.8 V, -0.35 V and 0 V vs. AgCl (for the 0 V experiment with and without two months storage inside a glovebox, with O_2 concentration below the detection limit of 20 ppm) was subtracted using anchor points above 400 cm^{-1} . A pseudo-Voigt fit with varying Gaussian (wG) and Lorentzian (wL) weighting was chosen for the spectra on the left-hand side and the average of the resulting values for wG and wL was used to fit the spectra again with shared values of $wG = 6.7$ and $wL = 12.9$ for the spectra on the right-hand side. The results are depicted in Figure S2, including the quality of the fits (R^2 coefficients).

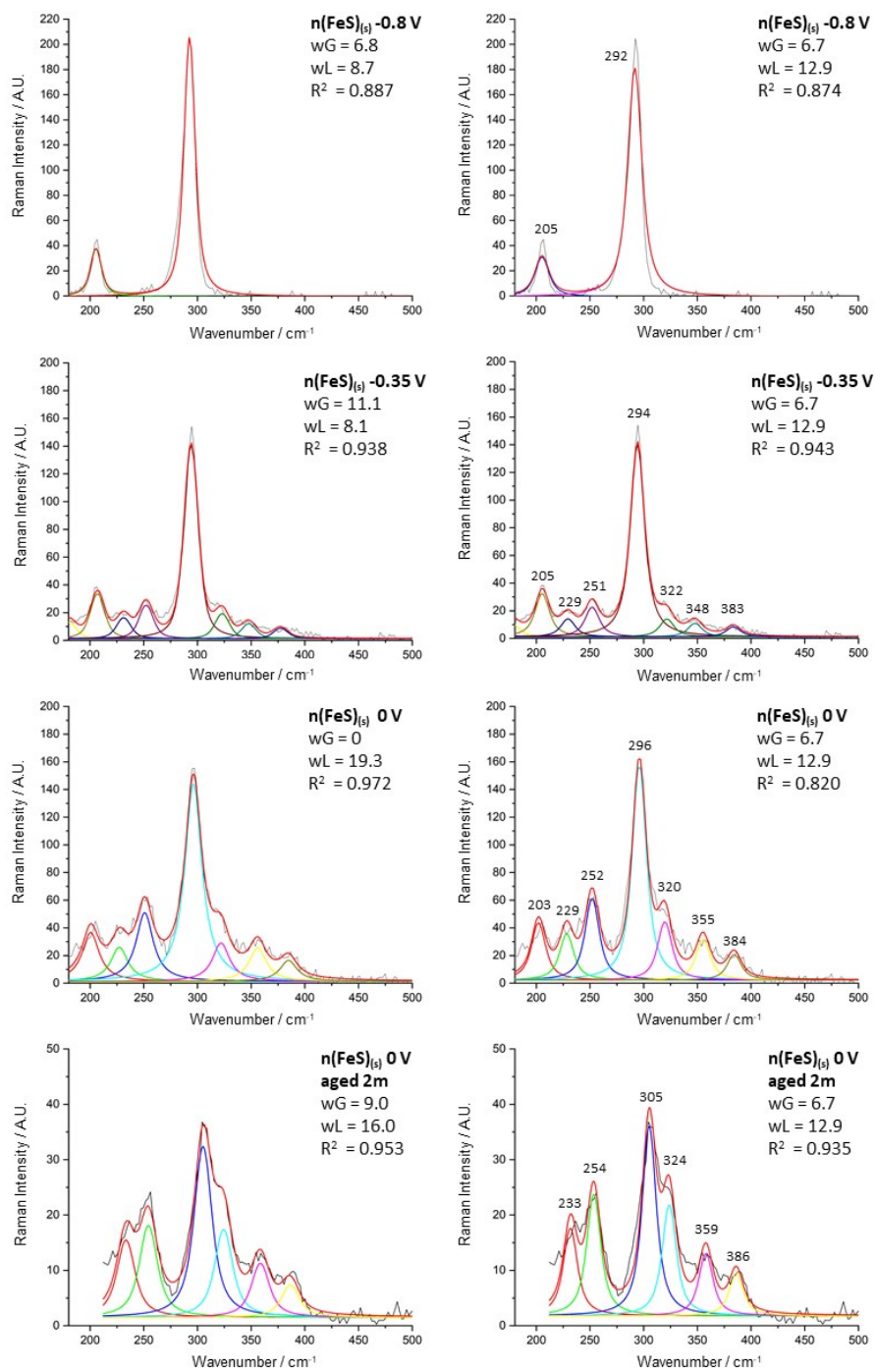


Figure S2, Peak-fitted Raman spectra of $n(\text{Fe}^{2+}\text{S}^{2-})_{(s)}$ with applied potentials of -0.8 V, -0.35 V, 0 V and 0 V with a 2 months aging process under anerobic conditions. The measured Raman spectra are displayed in black and the fitted spectra in red. For the spectra with the same Gaussian (wG) and Lorentzian weights (wL), the peak positions of the multicolored individual peaks are indicated above their respective peaks.

To demonstrate that the chosen level of theory [B(5%HF)P86/def2TZP/SMD(water)] produces experimentally sound, antiferromagnetically coupled iron centers in [2Fe-2S] rhombs, the Fe atomic spin densities from Mulliken population analysis are listed in Table S1.¹

Table S1: Two-electron, metal-centered redox series of the neutral [2Fe-2S] rhomb with representative structural features, bond covalency metrics (atomic spin density, SD), and Raman active vibrational modes (ν_i) denoted as strong, medium and weak intensity (s, m and w). The \pm sign for the spin densities indicate antiferromagnetically coupled Fe centers.

	Fe-S, Å	Fe-Fe, Å	S-S, Å	SD(Fe), e ⁻	ν_i (intensity)
¹ [2Fe-2S] ⁰	2.23	2.64	3.60	± 3.39	190(s) 244(m) 343(m)
² [2Fe-2S] ⁺	2.23, 2.25	2.74	3.53	3.84, -3.44	200(m) 289(m) 338(w) 365(s)
¹ [2Fe-2S] ²⁺	2.25	2.81	3.51	± 3.94	91(s) 204(w) 378(m)
¹ [2Fe-2S(SH)] ²⁺	2.41/2.38, 2.44	3.07	3.72	± 3.74	107(s) 184(m) 292(w) core only: 132(w) 191(s) 274(m) 308(w) 350(w)
¹ [8Fe-8S] ⁰	2.28	2.71	3.66	± 2.73	core only: 214(m) 259(s) 286(m) 305(w) 328(m)
² [8Fe-8S] ⁺	2.27	2.69	3.65	2.85, -2.63	core only: 224(w) 271(s) 301(m) 335(s)

Due to the symmetrized and truncated nature of the [2Fe-2S] rhombs, absolute agreement with the experimental Raman frequencies (as prepared $n(\text{Fe}^{2+}\text{S}_2^-)_{(s)}$; 207 and 292 cm^{-1} ; oxidized $n(\text{Fe}^{2+}\text{S}_2^-)_{(s)}$ at 0 V: 253 and 302 cm^{-1}) cannot be achieved. However, the relative changes among the Raman active modes reflect the increase in the rhomb stretching frequencies due to the increased strength of the Fe-S bonds upon oxidation. The most dominant change is the considerable shortening of the S-S distances, which opens up a pathway toward ligand-based redox chemistry. Higher covalency or increased ligand to metal (L→M) donation (as reflected by reduced atomic spin densities compared to the ionic ferrous (SD = 4) and ionic ferric (SD = 5)) in the oxidized form reduces the negative charge on the S centers, which decreases the ligand-to-ligand (L→L) repulsion and approximates an equilateral rhomb structure. The spin density changes can be correlated with the intensity changes of the XAS pre-edge features. Upon oxidation, a new electron hole is created in the Fe 3d manifold that is then partially occupied by electron donation from the S-ligands. Thus, instead of the formal 4, 4.5, and 5 electron holes, the effective spin densities are 3.4 for ferrous and 3.9 for ferric centers. The loss of 0.6 and 1.1 e⁻ from the ligands are due to S→Fe donation or the covalent interaction between the S-ligand and Fe center. This effectively radicalizes the S centers toward the persulfide electronic structure while being part of the oxidized rhomb. The [Fe²⁺Fe³⁺-2S²⁻]⁺ rhomb and [Fe²⁺-(S-S)³⁻-Fe²⁺]⁺ chain are isoelectronic.

The persulfide ligand can be terminal or bridging between the iron centers and can coordinate end-on or side-on. The replacement of the bridging S²⁻ with a S₂²⁻ ligand causes major structural changes between the [2Fe-2S] and [2Fe-2S(SH)]²⁺ as shown in Table S1, since the reduced nucleophilicity of the S-ligand in the latter drastically elongates all intramolecular distances. The Fe spin density increases by 0.35 e⁻ toward the ionic limit, which is the clear indication of reduced Fe-S covalency and resulting in a significantly diminished XANES spectral intensities at the S K-edge. The Raman active normal modes shift and the intensities redistribute in a complex manner that limits the direct comparison of the Raman features between the clusters with different S-ligands.

To evaluate the employed level of theory in predicting Raman spectra, we utilized the scaled quantum mechanical force field approach to determine the deviation from the experimentally obtained Raman spectra.^{2,3} Table S2 depicts the

scale and shift parameters obtained in reference to the Raman spectrum of $n(\text{Fe}^{2+}\text{S}^{2-})_{(\text{s})}$ at 0V, which was stored under anaerobic conditions for 2 months.

Table S2: Evaluation of scaled quantum mechanical force field parameters for the simulation of Raman spectra of [2Fe-2S] rhomb-based models of mackinawite and mackinawite-like nanoparticles.

				average
Experimental, cm^{-1}	207	253	292	251
Periodic model, cm^{-1}	215	265	305	262
shift, cm^{-1}	11			11
Scale	95%	96%	96%	96%
SQM-FF error, cm^{-1}	-12	-10	-11	r.m.s.:11
Molecular cluster, cm^{-1}	214	259	328	267
shift, cm^{-1}	16			16
Scale	92%	94%	95%	94%
SQM-FF error, cm^{-1}	-22	-26	0	r.m.s.:19

3. Calculated Raman spectra of [2Fe2S] rhombs

The following Raman spectra were computed using B(5%HF)P86/def2TZP/SMD(water) as implemented in Gaussian16 Rev.C01 and the core-extracted FeS rhombs were computed using Gaussian09 Rev.D01. The resulting Raman activities were converted into Raman intensities using the following equation⁴:

$$\frac{d\sigma}{d\Omega} = \frac{2^4 \pi^4}{45} \frac{(v_0 - v_j)^4}{1 - \exp\left(-\frac{hcv_j}{k_B T}\right)} \frac{h}{8\pi^2 cv_j}$$

where k_B is the Boltzmann constant, h the Planck constant, T the temperature (298.15K), c the speed of light in cm s^{-1} , and v_j and v_0 are the Raman active mode and the wavelength of the laser in cm^{-1} (18800) respectively. The resulting Raman intensities were broadened using a pseudo-Voigt distribution:

$$y = a_0 \left[\frac{\frac{a_3 \sqrt{\ln 2}}{a_2 \sqrt{\pi}} \exp\left(-4 \ln 2 \left(\frac{x - a_1}{a_2}\right)^2\right) + \frac{1 - a_3}{\pi a_2 \left[1 + 4 \left(\frac{x - a_1}{a_2}\right)^2\right]}}{\frac{a_3 \sqrt{\ln 2}}{a_2 \sqrt{\pi}} + \frac{1 - a_3}{\pi a_2}} \right]$$

a_0 = amplitude
 a_1 = center
 a_2 = width (>0)
 a_3 = shape ($\geq 0, \leq 1$)

with $a_2 = 13$ and $a_3 = 0.05$, which was derived from the best fit of the Raman band of $n(\text{Fe}^{2+}\text{S}^{2-})_{(\text{s})}$ at -0.8 V at 292 cm^{-1} .

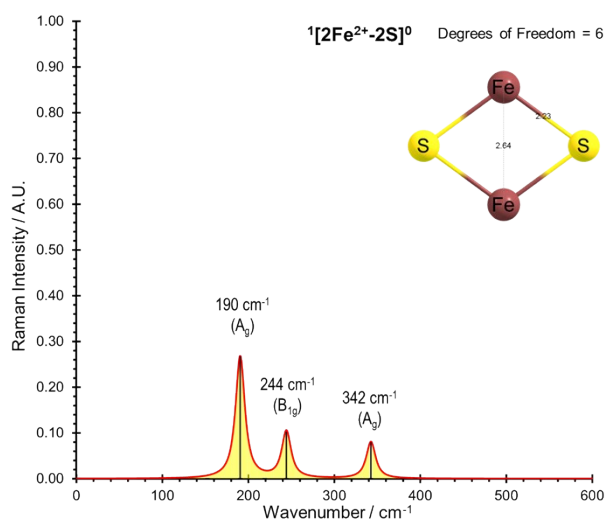


Figure S3. Calculated Raman spectrum of $1[2\text{Fe}-2\text{S}]^0$. The intensities for 6 degrees of freedom were scaled to the Raman band of $1[2\text{Fe}-2\text{S}]^{2+}$ at 91 cm^{-1} .

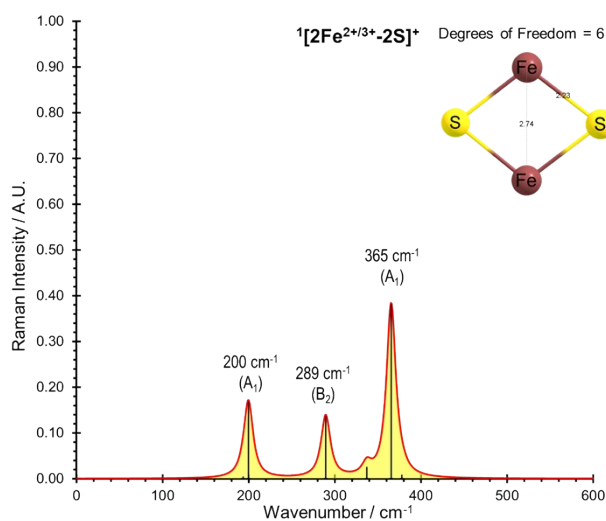


Figure S4. Calculated Raman spectrum of $1[2\text{Fe}-2\text{S}]^+$. The intensities for 6 degrees of freedom were scaled to the Raman band of $1[2\text{Fe}-2\text{S}]^{2+}$ at 91 cm^{-1} .

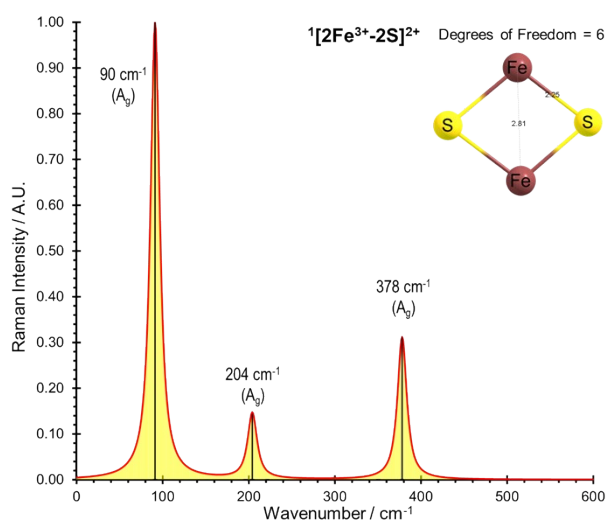


Figure S5. Calculated Raman spectrum of $1[2\text{Fe}-2\text{S}]^{2+}$. The intensities for 6 degrees of freedom were scaled to the Raman band at 91 cm^{-1} .

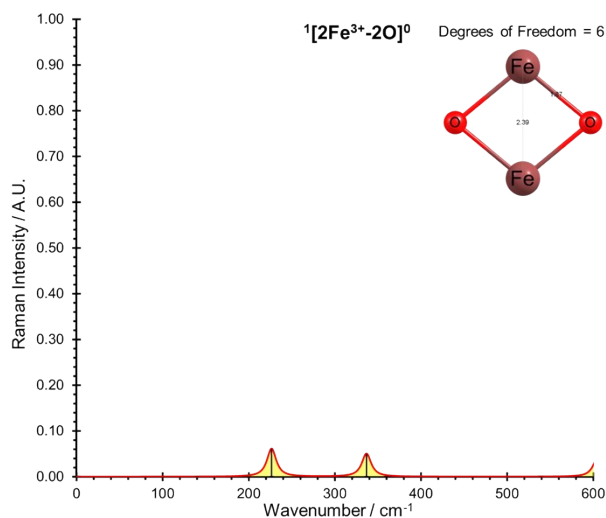


Figure S6. Calculated Raman spectrum of $^1[2\text{Fe}\text{-}2\text{O}]^0$. The intensities for 6 degrees of freedom were scaled to the Raman band of $^1[2\text{Fe}\text{-}2\text{S}]^{2+}$ at 91cm^{-1} .

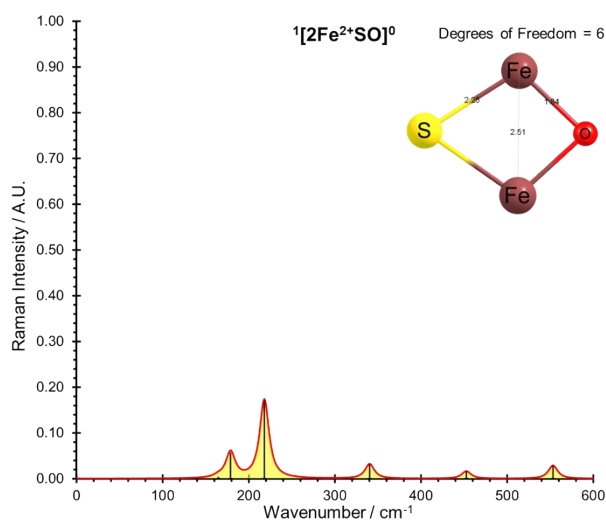


Figure S7. Calculated Raman spectrum of $^1[2\text{Fe}\text{-}\text{SO}]^0$. The intensities for 6 degrees of freedom were scaled to the Raman band of $^1[2\text{Fe}\text{-}2\text{S}]^{2+}$ at 91cm^{-1} .

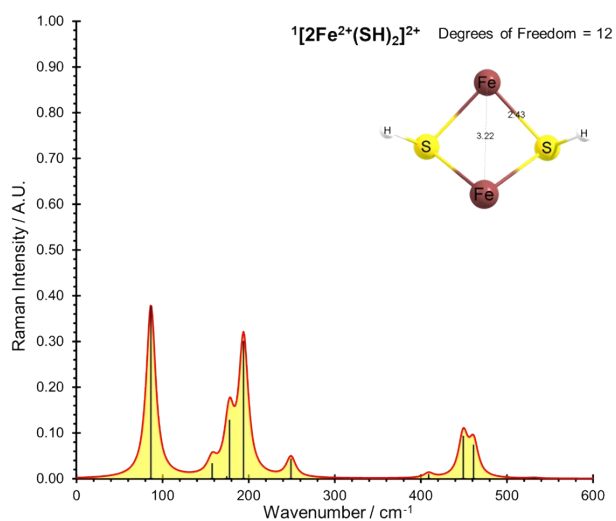


Figure S8. Calculated Raman spectrum of $^1[2\text{Fe}(\text{SH})_2]^{2+}$. The intensities for 12 degrees of freedom were scaled to the Raman band of $^1[2\text{Fe}\text{-}(\text{SH})_2]^{3+}$ at 233cm^{-1} .

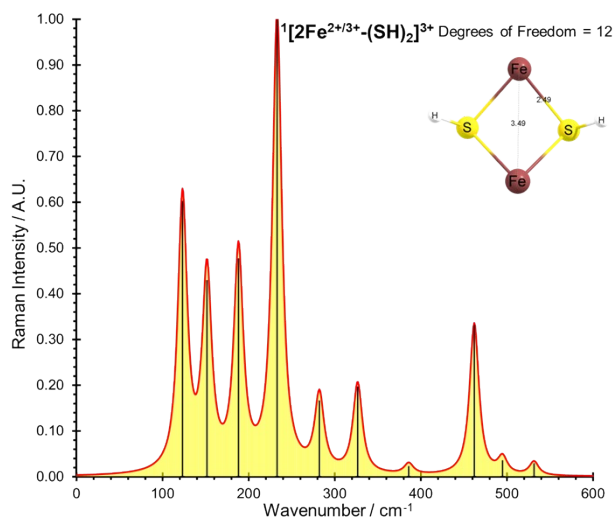


Figure S9. Calculated Raman spectrum of $^1[2\text{Fe}^{2+/3+}(\text{SH})_2]^{3+}$. The intensities for 12 degrees of freedom were scaled to the Raman band of $^1[2\text{Fe}(\text{SH})_2]^{3+}$ at 233 cm^{-1} .

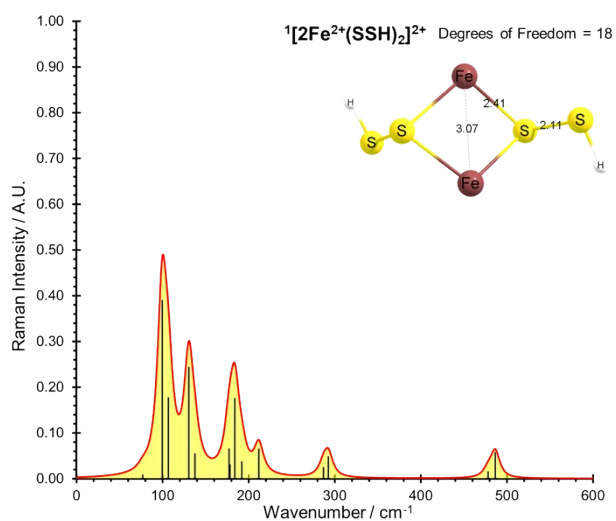


Figure S10. Calculated Raman spectrum of $^1[2\text{Fe}(\text{SSH})_2]^{2+}$. The intensities for 18 degrees of freedom were scaled to the Raman band of $^1[2\text{Fe}(\text{SSH})_2]^{3+}$ at 107 cm^{-1} .

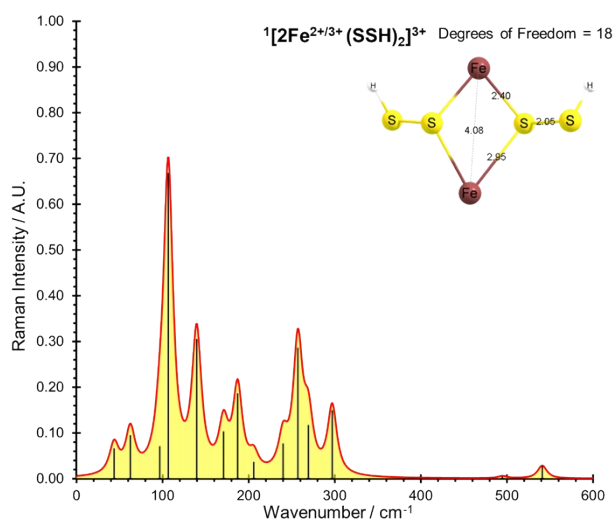


Figure S11. Calculated Raman spectrum of $^1[2\text{Fe}(\text{SSH})_2]^{3+}$. The intensities for 12 degrees of freedom were scaled to the Raman band of $^1[2\text{Fe}(\text{SSH})_2]^{3+}$ at 107 cm^{-1} .

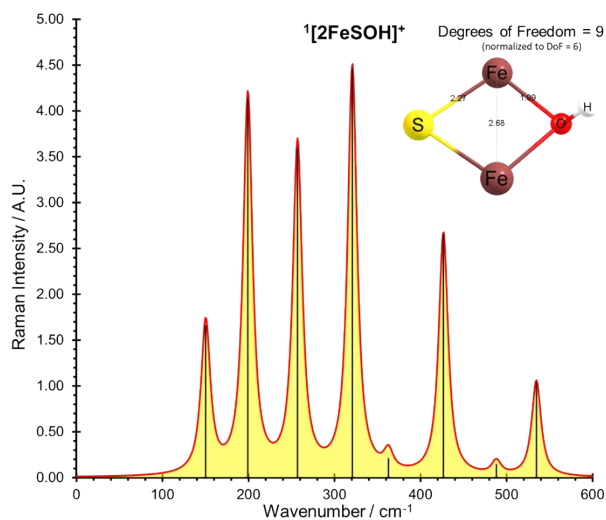


Figure S12. Calculated Raman spectrum of $^1[2\text{FeSOH}]^+$. The intensities for 9 degrees of freedom were scaled to the Raman band of $^1[2\text{Fe}(\text{SH})_2]^{3+}$ at 233 cm^{-1} (degrees of freedom = 6).

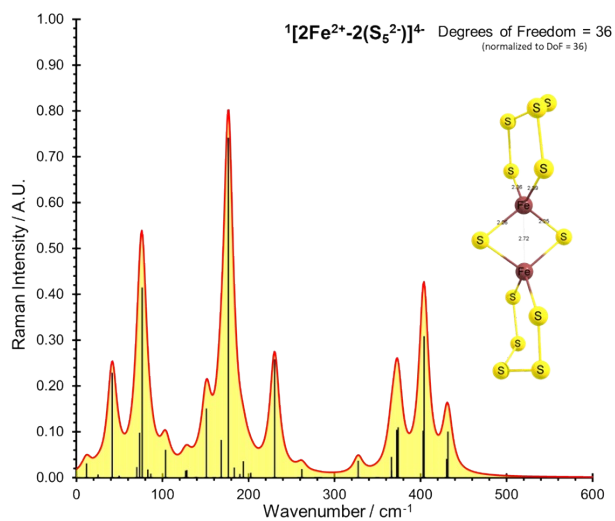


Figure S13. Calculated Raman spectrum of $^1[2\text{Fe}-2(\text{S}_5^{2-})]^{4+}$. The intensities for 36 degrees of freedom were scaled to the Raman band of $^2\{[2\text{Fe}-2(\text{S}_5^{2-})](\text{SH})_2\}^-$ at 43 cm^{-1} .

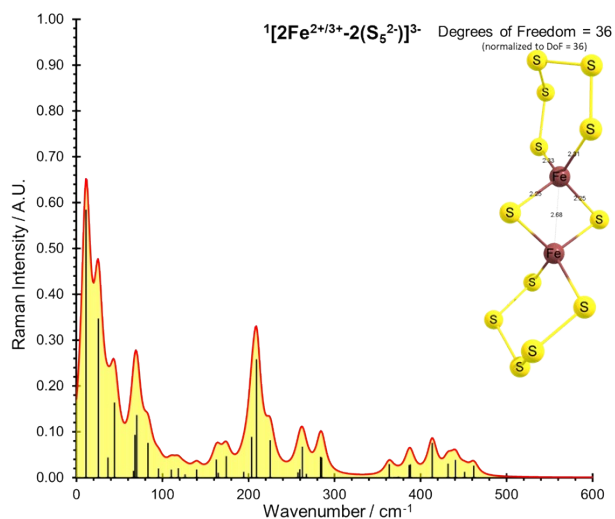


Figure S14. Calculated Raman spectrum of $^2[2\text{Fe}-2(\text{S}_5^{2-})]^{3-}$. The intensities for 36 degrees of freedom were scaled to the Raman band of $^2\{[2\text{Fe}-2(\text{S}_5^{2-})](\text{SH})_2\}^-$ at 43 cm^{-1} .

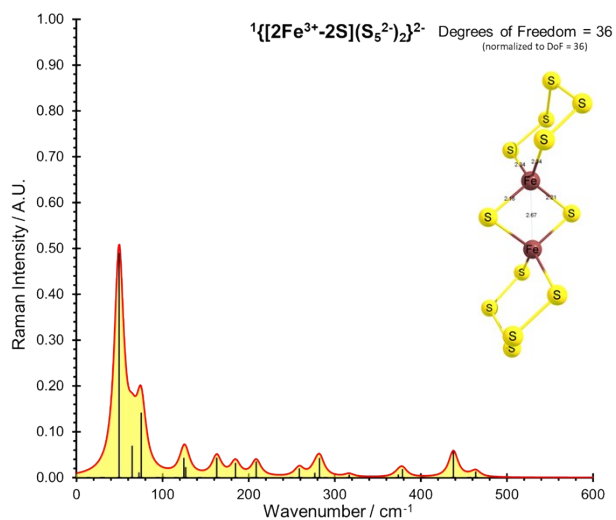


Figure S15. Calculated Raman spectrum of $^1\{[2\text{Fe}\cdot 2\text{S}](\text{S}_5^{2-})_2\}^{2-}$. The intensities for 36 degrees of freedom were scaled to the Raman band of $^2\{[2\text{Fe}\cdot 2(\text{S}_5^{2-})](\text{SH})_2\}^-$ at 43 cm^{-1} .

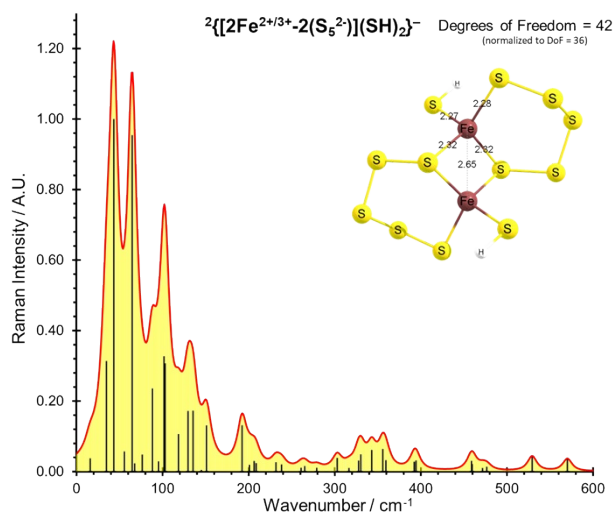


Figure S16. Calculated Raman spectrum of $^2\{[2\text{Fe}\cdot 2(\text{S}_5^{2-})](\text{SH})_2\}^-$. The intensities for 36 degrees of freedom were scaled to the Raman band at 43 cm^{-1} .

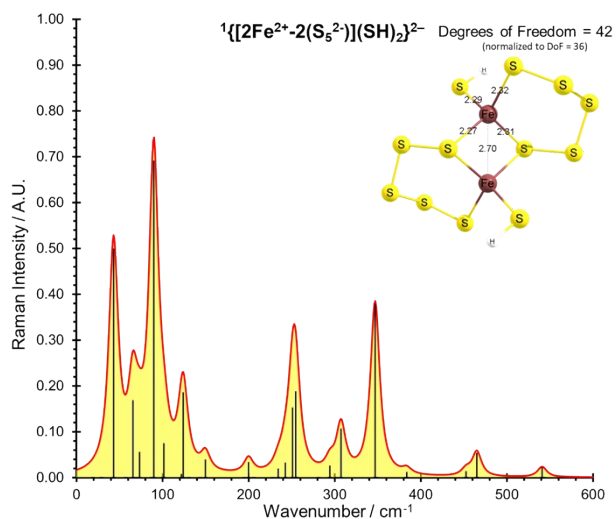


Figure S17. Calculated Raman spectrum of $^1\{[2\text{Fe}\cdot 2(\text{S}_5^{2-})](\text{SH})_2\}^{2-}$. The intensities for 36 degrees of freedom were scaled to the Raman band of $^2\{[2\text{Fe}\cdot 2(\text{S}_5^{2-})](\text{SH})_2\}^-$ at 43 cm^{-1} .

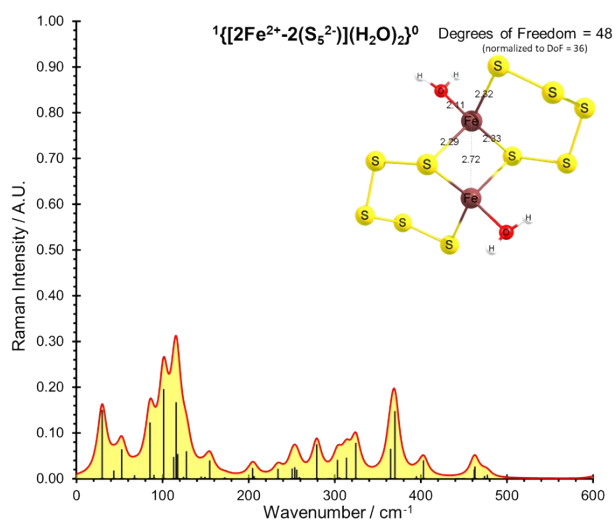


Figure S18. Calculated Raman spectrum of $^1\{[2\text{Fe}^{2+}-2(\text{S}_5^{2-})](\text{H}_2\text{O})_2\}^0$. The intensities for 36 degrees of freedom were scaled to the Raman band of $^2\{[2\text{Fe}^{2+}-2(\text{S}_5^{2-})](\text{SH})_2\}^-$ at 43 cm^{-1} .

4. Calculated Raman spectra of FeS nanoparticles

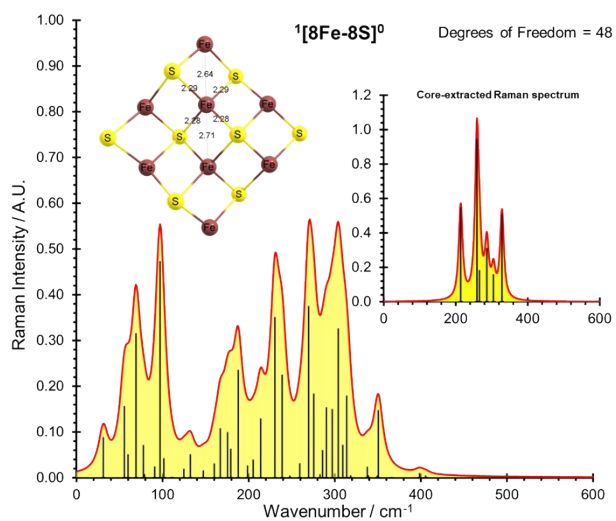


Figure S19. Calculated Raman spectrum of $^1[8\text{Fe}-8\text{S}]^0$. The intensities for 48 degrees of freedom were scaled to the Raman band of $^2[8\text{Fe}-8\text{S}]^{+1}$ (1b) at 56 cm^{-1} . The inset shows the core-extracted central $[2\text{Fe}-2\text{S}]$ rhomb scaled to vibrational mode at 291 cm^{-1} of the central rhomb of the $^1\{[2\text{Fe}-2\text{S}]\times[6\text{Fe}-6\text{SH}](\text{S}_5)_2(\text{SH})_4\}^0$ nanoparticle.

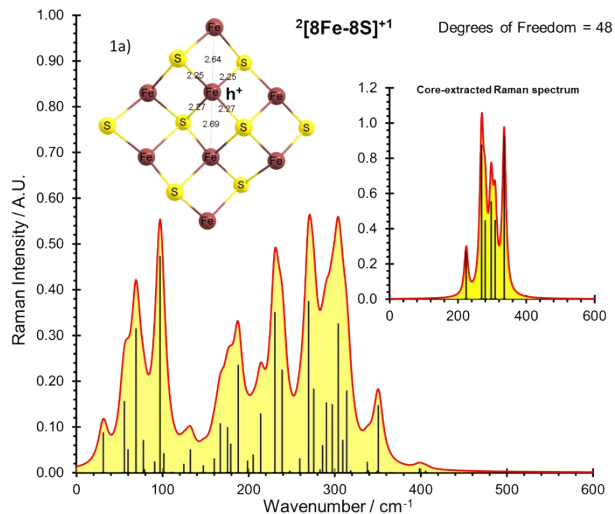


Figure S20. Calculated Raman spectrum of ${}^2[8\text{Fe}-8\text{S}]^+$ 1a), with the electron located on the central rhomb. The intensities for 48 degrees of freedom were scaled to the Raman band of ${}^2[8\text{Fe}-8\text{S}]^+$ (1b) at 56 cm^{-1} . The inset shows the core-extracted central $[2\text{Fe}-2\text{S}]$ rhomb scaled to vibrational mode at 291 cm^{-1} of the central rhomb of ${}^1\{[2\text{Fe}-2\text{S}]\times[6\text{Fe}-6\text{SH}](\text{S}_5)_2(\text{SH})_4\}^0$. The location of the electron hole (h^+) at the start of the optimization is indicated next to the corresponding Fe atom.

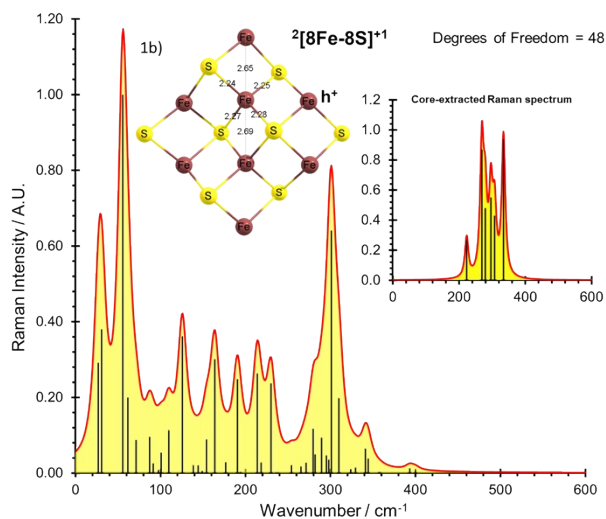


Figure S21. Calculated Raman spectrum of ${}^2[8\text{Fe}-8\text{S}]^+$ 1b), with the electron located at the edge of the structure on a $\mu^3\text{-Fe}$. The intensities for 48 degrees of freedom were scaled to the Raman band of ${}^2[8\text{Fe}-8\text{S}]^+$ (1b) at 56 cm^{-1} . The inset shows the core-extracted central $[2\text{Fe}-2\text{S}]$ rhomb scaled to vibrational mode at 291 cm^{-1} of the central rhomb of ${}^1\{[2\text{Fe}-2\text{S}]\times[6\text{Fe}-6\text{SH}](\text{S}_5)_2(\text{SH})_4\}^0$. The location of the electron hole (h^+) at the start of the optimization is indicated next to the corresponding Fe atom.

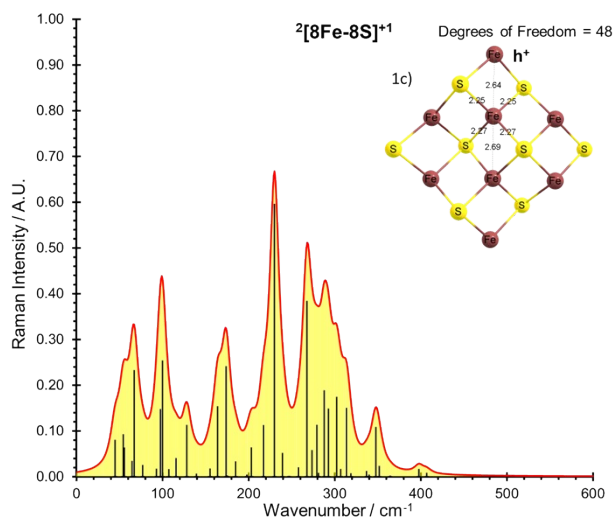


Figure S22. Calculated Raman spectrum of ${}^2[8\text{Fe}-8\text{S}]^+$ 1c), with the electron located on a bridging $\mu^2\text{-Fe}$. The intensities for 48 degrees of freedom were scaled to the Raman band of ${}^2[8\text{Fe}-8\text{S}]^+$ (1b) at 56 cm^{-1} . The location of the electron hole (h^+) at the start of the optimization is indicated next to the corresponding Fe atom.

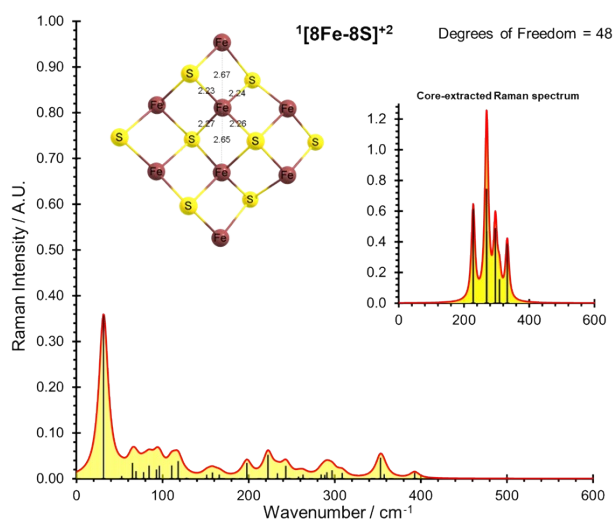


Figure S23. Calculated Raman spectrum of $^1[8\text{Fe-}8\text{S}]^{2+}$. The intensities for 48 degrees of freedom were scaled to the Raman band of $^2[8\text{Fe-}8\text{S}]^+$ (1b) at 56 cm^{-1} . The inset shows the core-extracted central $[2\text{Fe-}2\text{S}]$ rhomb scaled to vibrational mode at 291 cm^{-1} of the central rhomb of the $^1\{[2\text{Fe-}2\text{S}]\times[6\text{Fe-}6\text{SH}](\text{S}_5)_2(\text{SH})_4\}^0$ nanoparticle.

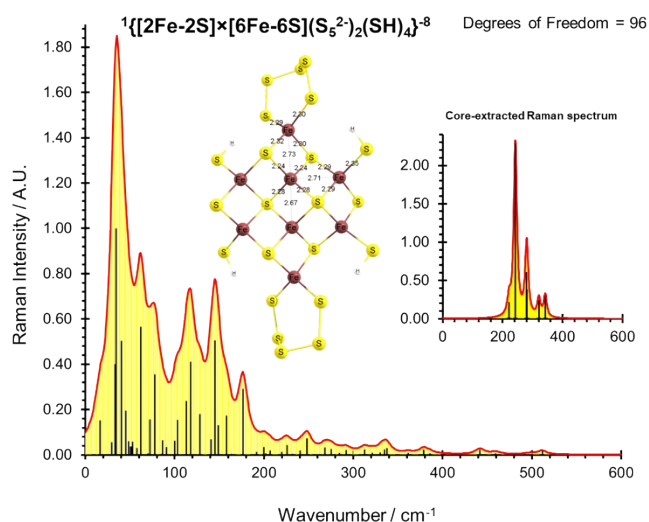


Figure S24. Calculated Raman spectrum of $^1\{[8\text{Fe-}8\text{S}](\text{S}_5^{2-})_2(\text{SH})_4\}^{8-}$. The intensities for 96 degrees of freedom were scaled to the Raman band of $^2\{[8\text{Fe-}8\text{S}](\text{S}_5)_2(\text{SH})_4\}^{6-}$ at 9 cm^{-1} . The inset shows the core-extracted central $[2\text{Fe-}2\text{S}]$ rhomb scaled to vibrational mode at 291 cm^{-1} of the central rhomb of $^1\{[2\text{Fe-}2\text{S}]\times[6\text{Fe-}6\text{SH}](\text{S}_5)_2(\text{SH})_4\}^0$.

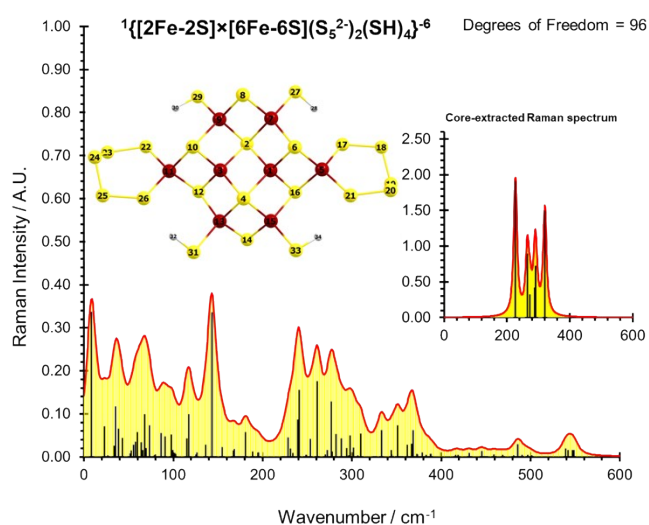


Figure S25. Calculated Raman spectrum of $^1\{[8\text{Fe-}8\text{S}](\text{S}_5^{2-})_2(\text{SH})_4\}^{6-}$. The intensities for 96 degrees of freedom were scaled to the Raman band at 9 cm^{-1} . The inset shows the core-extracted central $[2\text{Fe-}2\text{S}]$ rhomb scaled to vibrational mode at 291 cm^{-1} of the central rhomb of $^1\{[2\text{Fe-}2\text{S}]\times[6\text{Fe-}6\text{SH}](\text{S}_5)_2(\text{SH})_4\}^0$.

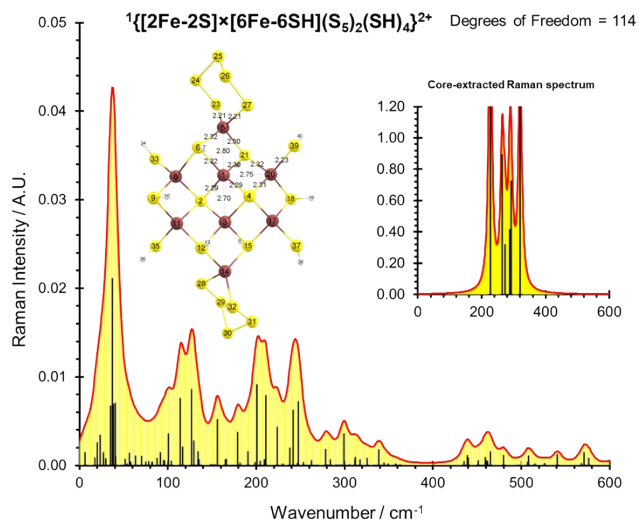


Figure S26. Calculated Raman spectrum of $1\{[2\text{Fe}-2\text{S}]\times[6\text{Fe}-6\text{SH}](\text{S}_5)_2(\text{SH})_4\}^{2+}$. The intensities for 114 degrees of freedom were scaled to the Raman band of $2\{[8\text{Fe}-8\text{S}](\text{S}_5)_2(\text{SH})_4\}^+$ at 35 cm^{-1} . The inset shows the core-extracted central $[2\text{Fe}-2\text{S}]$ rhomb scaled to vibrational mode of the central rhomb at 291 cm^{-1} of the $1\{[2\text{Fe}-2\text{S}]\times[6\text{Fe}-6\text{SH}](\text{S}_5)_2(\text{SH})_4\}^0$ nanoparticle.

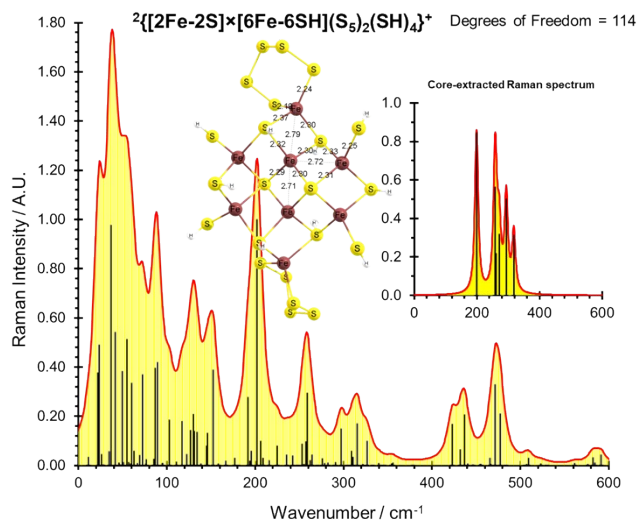


Figure S27. Calculated Raman spectrum of $2\{[2\text{Fe}-2\text{S}]\times[6\text{Fe}-6\text{SH}](\text{S}_5)_2(\text{SH})_4\}^+$. The intensities for 114 degrees of freedom were scaled to the Raman band at 35 cm^{-1} . The inset shows the core-extracted central $[2\text{Fe}-2\text{S}]$ rhomb scaled to vibrational mode of the central rhomb at 291 cm^{-1} of the $1\{[2\text{Fe}-2\text{S}]\times[6\text{Fe}-6\text{SH}](\text{S}_5)_2(\text{SH})_4\}^0$ nanoparticle.

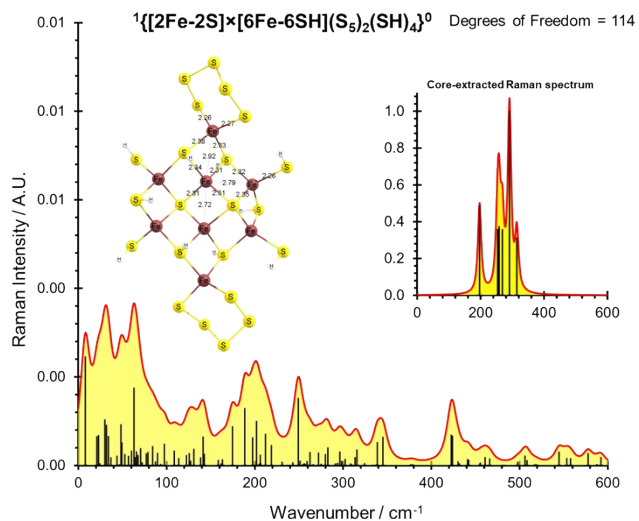


Figure S28. Calculated Raman spectrum of $1\{[2\text{Fe}-2\text{S}]\times[6\text{Fe}-6\text{SH}](\text{S}_5)_2(\text{SH})_4\}^0$. The intensities for 114 degrees of freedom were scaled to the Raman band of $2\{[8\text{Fe}-8\text{S}](\text{S}_5)_2(\text{SH})_4\}^+$ at 35 cm^{-1} . The inset shows the core-extracted central $[2\text{Fe}-2\text{S}]$ rhomb scaled to vibrational mode of the central rhomb at 291 cm^{-1} .

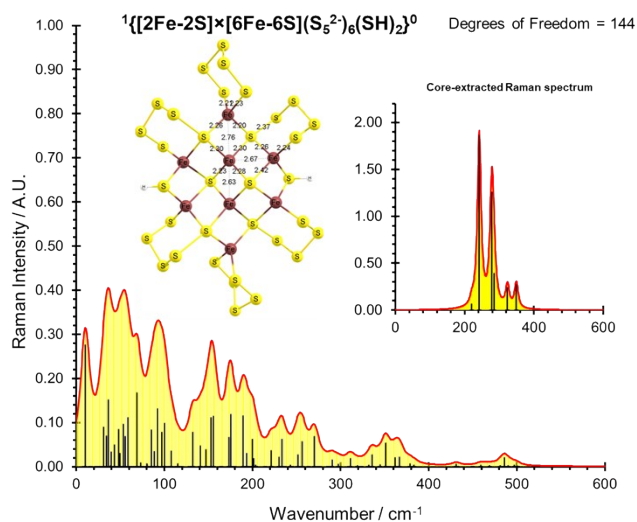


Figure S29. Calculated Raman spectrum of $^1\{[8\text{Fe}-8\text{S}](\text{S}_5^{2-})_6(\text{SH})_2\}$. The intensities for 144 degrees of freedom were scaled to the Raman band of $^1\{[8\text{Fe}-8\text{S}](\text{S}_5^{2-})_6(\text{SH})_2\}^{2-}$ at 35 cm^{-1} . The inset shows core-extracted central $[2\text{Fe}-2\text{S}]$ rhomb scaled to vibrational mode at 291 cm^{-1} of the central rhomb of the $^1\{[2\text{Fe}-2\text{S}]\times[6\text{Fe}-6\text{SH}](\text{S}_5)_2(\text{SH})_4\}^0$ nanoparticle.

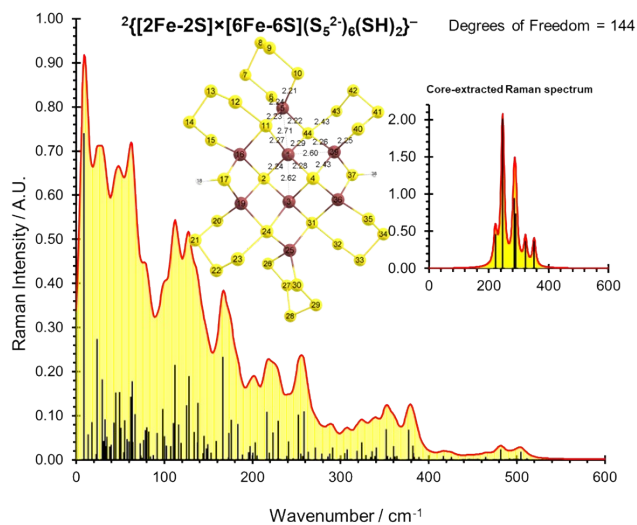


Figure S30. Calculated Raman spectrum of $^1\{[8\text{Fe}-8\text{S}](\text{S}_5^{2-})_6(\text{SH})_2\}^-$. The intensities for 144 degrees of freedom were scaled to the Raman band of $^1\{[8\text{Fe}-8\text{S}](\text{S}_5^{2-})_6(\text{SH})_2\}^{2-}$ at 35 cm^{-1} . The inset shows core-extracted central $[2\text{Fe}-2\text{S}]$ rhomb scaled to vibrational mode at 291 cm^{-1} of the central rhomb of the $^1\{[2\text{Fe}-2\text{S}]\times[6\text{Fe}-6\text{SH}](\text{S}_5)_2(\text{SH})_4\}^0$ nanoparticle.

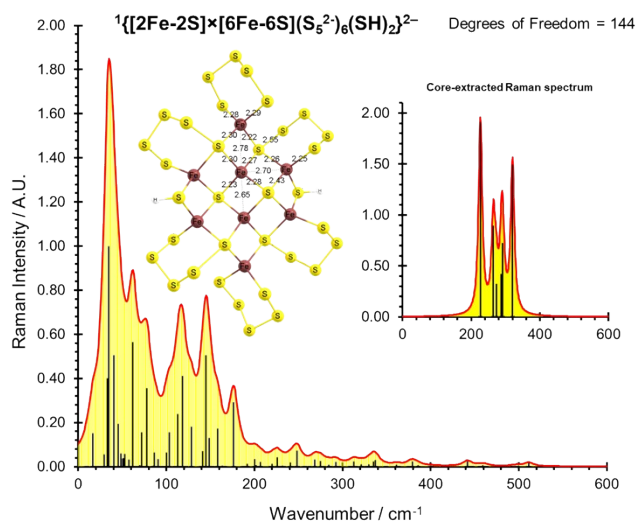


Figure S31. Calculated Raman spectrum of $^1\{[8\text{Fe}-8\text{S}](\text{S}_5^{2-})_6(\text{SH})_2\}^{2-}$. The intensities for 144 degrees of freedom were scaled to the Raman band of $^1\{[8\text{Fe}-8\text{S}](\text{S}_5^{2-})_6(\text{SH})_2\}^{2-}$ at 35 cm^{-1} . The inset shows core-extracted central $[2\text{Fe}-2\text{S}]$ rhomb scaled to vibrational mode at 291 cm^{-1} of the central rhomb of the $^1\{[2\text{Fe}-2\text{S}]\times[6\text{Fe}-6\text{SH}](\text{S}_5)_2(\text{SH})_4\}^0$ nanoparticle.

5. Calculated Raman spectra of FeS complexes

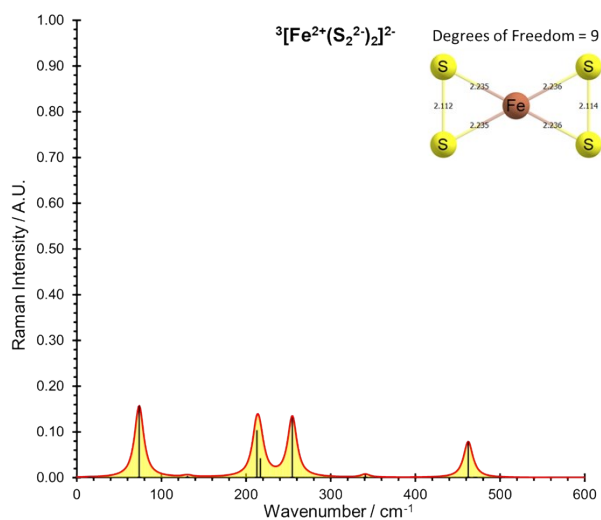


Figure S32. Calculated Raman spectrum of $^3[\text{Fe}^{2+}(\text{S}_2^{2-})_2]^{2-}$. The intensities for 9 degrees of freedom were scaled to the Raman band of $^2[[8\text{Fe}^{3+}(\text{S}_2^{2-})_2]^-$ at 248 cm^{-1} .

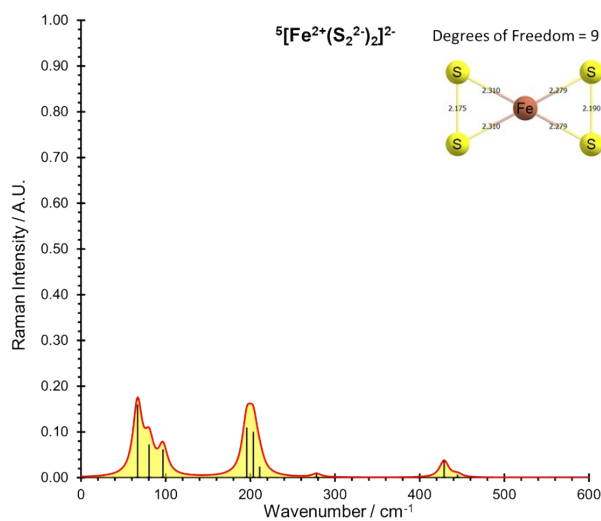


Figure S33. Calculated Raman spectrum of $^5[\text{Fe}^{2+}(\text{S}_2^{2-})_2]^{2-}$. The intensities for 9 degrees of freedom were scaled to the Raman band of $^2[[8\text{Fe}^{3+}(\text{S}_2^{2-})_2]^-$ at 248 cm^{-1} .

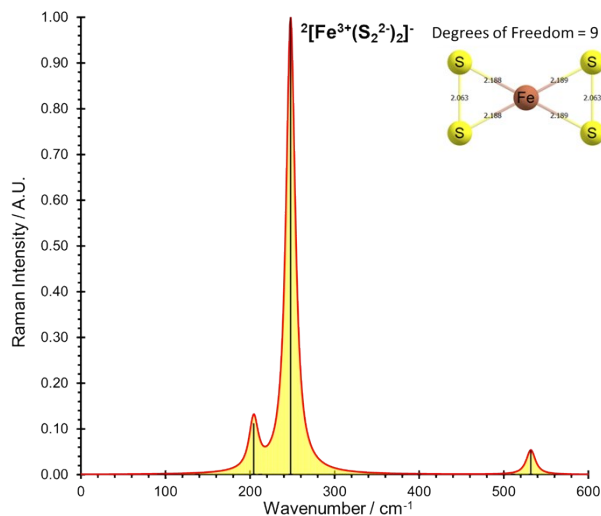


Figure S34. Calculated Raman spectrum of $2[\text{Fe}^{3+}(\text{S}_2^{2-})_2]$. The intensities for 9 degrees of freedom were scaled to the Raman band at 248 cm^{-1} .

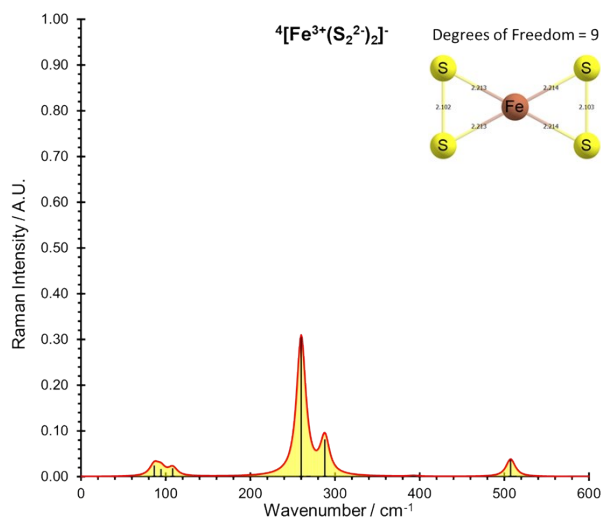


Figure S35. Calculated Raman spectrum of $4[\text{Fe}^{3+}(\text{S}_2^{2-})_2]$. The intensities for 9 degrees of freedom were scaled to the Raman band of $2\{[8\text{Fe}^{3+}(\text{S}_2^{2-})_2]\}$ at 248 cm^{-1} .

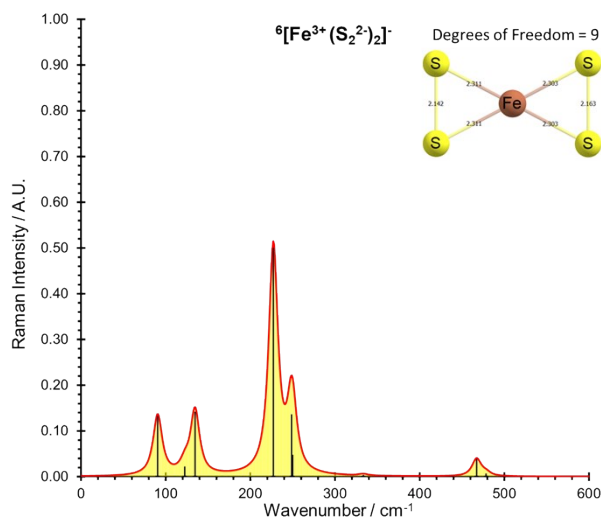


Figure S36. Calculated Raman spectrum of $6[\text{Fe}^{3+}(\text{S}_2^{2-})_2]$. The intensities for 9 degrees of freedom were scaled to the Raman band of $2\{[8\text{Fe}^{3+}(\text{S}_2^{2-})_2]\}$ at 248 cm^{-1} .

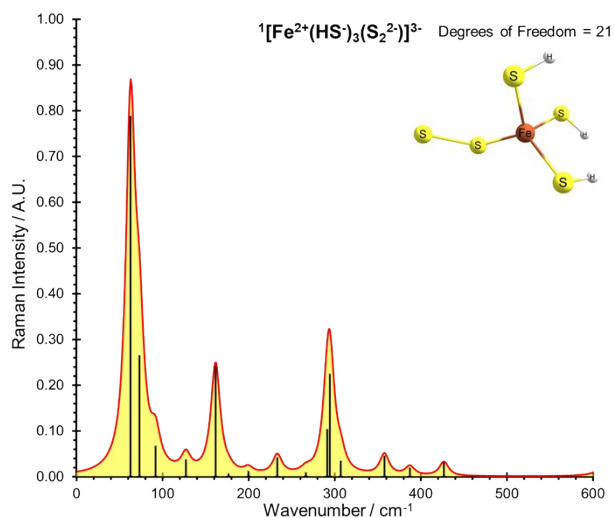


Figure S37. Calculated Raman spectrum of $^1[\text{Fe}^{2+}(\text{HS})_3(\text{S}_2^{2-})]^{3-}$. The intensities for 21 degrees of freedom were scaled to the Raman band of $^1[\text{Fe}^{2+}(\text{HS})_3(\text{S}_2^{2-})]^{3-}$ at 2216 cm^{-1} .

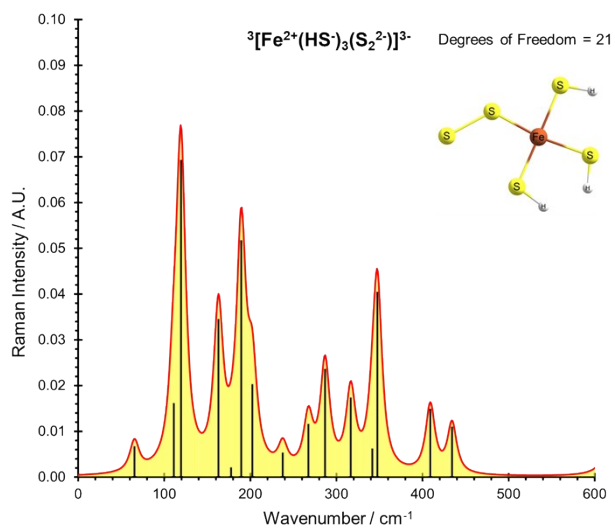


Figure S38. Calculated Raman spectrum of $^3[\text{Fe}^{2+}(\text{HS})_3(\text{S}_2^{2-})]^{3-}$. The intensities for 21 degrees of freedom were scaled to the Raman band of $^1[\text{Fe}^{2+}(\text{HS})_3(\text{S}_2^{2-})]^{3-}$ at 2216 cm^{-1} .

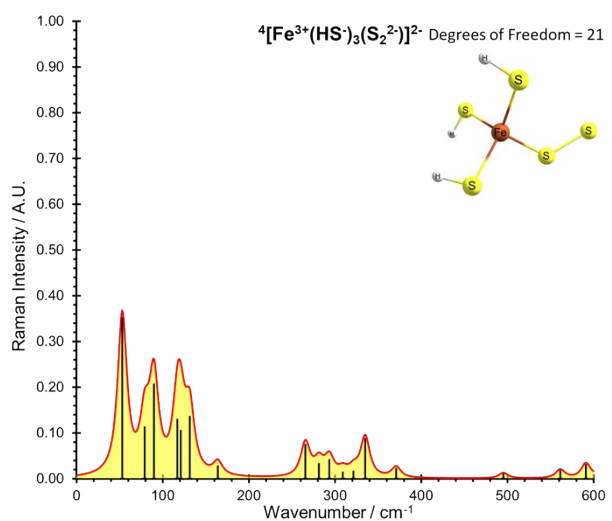


Figure S39. Calculated Raman spectrum of $^4[\text{Fe}^{3+}(\text{HS})_3(\text{S}_2^{2-})]^{2-}$. The intensities for 21 degrees of freedom were scaled to the Raman band of $^1[\text{Fe}^{2+}(\text{HS})_3(\text{S}_2^{2-})]^{3-}$ at 2216 cm^{-1} .

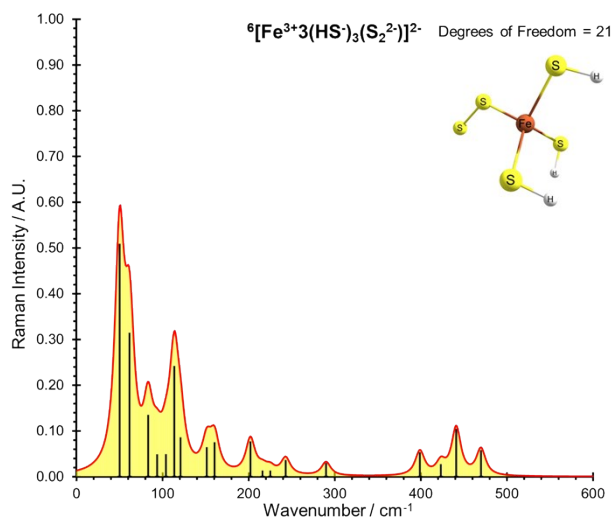


Figure S40. Calculated Raman spectrum of ${}^6[\text{Fe}^{3+}3(\text{HS}^-)_3(\text{S}_2^{2-})]^{2-}$. The intensities for 21 degrees of freedom were scaled to the Raman band of ${}^1[\text{Fe}^{2+}(\text{HS}^-)_3(\text{S}_2^{2-})]^{3-}$ at 2216 cm^{-1} .

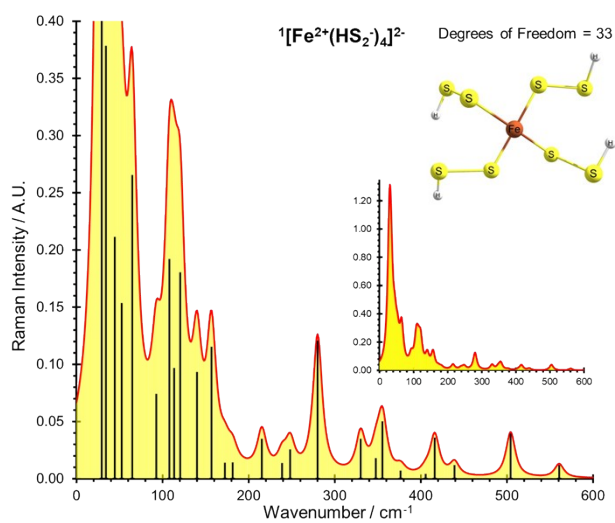


Figure S41. Calculated Raman spectrum of ${}^1[\text{Fe}^{2+}(\text{HS}_2^-)_4]^{2-}$. The inset shows intensities for 33 degrees of freedom scaled to the Raman band of at 29 cm^{-1} .

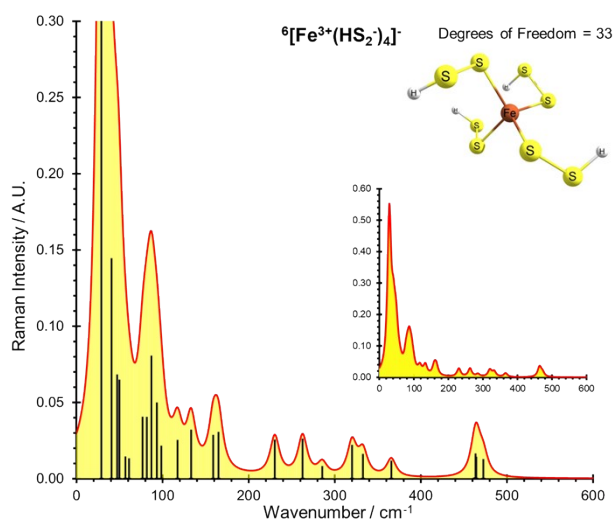


Figure S42. Calculated Raman spectrum of ${}^6[\text{Fe}^{3+}(\text{HS}_2^-)_4]^{-}$. The inset shows intensities for 33 degrees of freedom scaled to the Raman band of ${}^1[\text{Fe}^{2+}(\text{HS}_2^-)_4]^{2-}$ at 29 cm^{-1} .

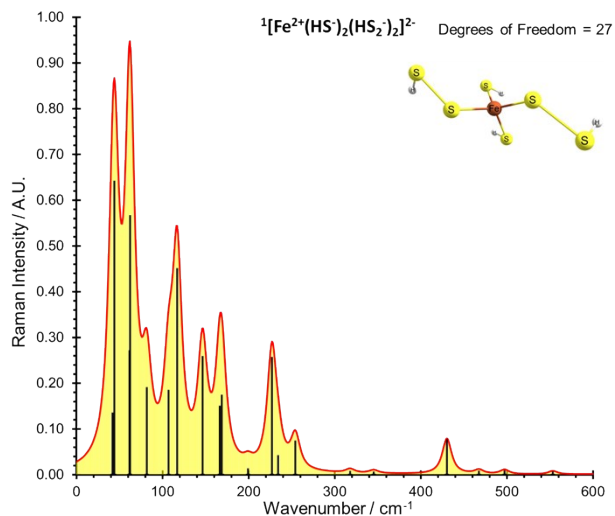


Figure S43. Calculated Raman spectrum of $^1[\text{Fe}^{2+}(\text{HS}^-)_2(\text{HS}_2^-)_2]^{2-}$. The intensities for 27 degrees of freedom were scaled to the Raman band of $^6[\text{Fe}^{3+}(\text{HS}^-)_2(\text{HS}_2^-)_2]^-$ at 30 cm^{-1} .

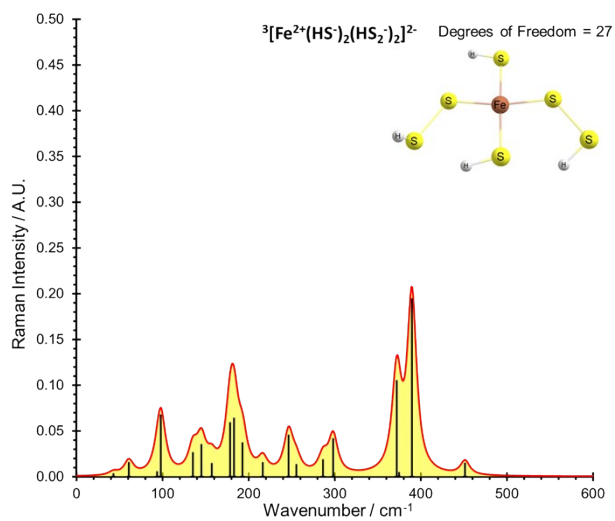


Figure S44. Calculated Raman spectrum of $^3[\text{Fe}^{2+}(\text{HS}^-)_2(\text{HS}_2^-)_2]^{2-}$. The intensities for 27 degrees of freedom were scaled to the Raman band of $^6[\text{Fe}^{3+}(\text{HS}^-)_2(\text{HS}_2^-)_2]^-$ at 30 cm^{-1} .

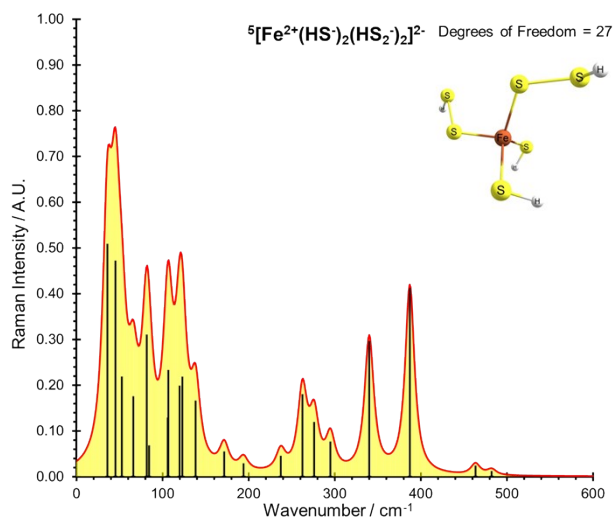


Figure S45. Calculated Raman spectrum of $^5[\text{Fe}^{2+}(\text{HS}^-)_2(\text{HS}_2^-)_2]^{2-}$. The intensities for 27 degrees of freedom were scaled to the Raman band of $^6[\text{Fe}^{3+}(\text{HS}^-)_2(\text{HS}_2^-)_2]^-$ at 30 cm^{-1} .

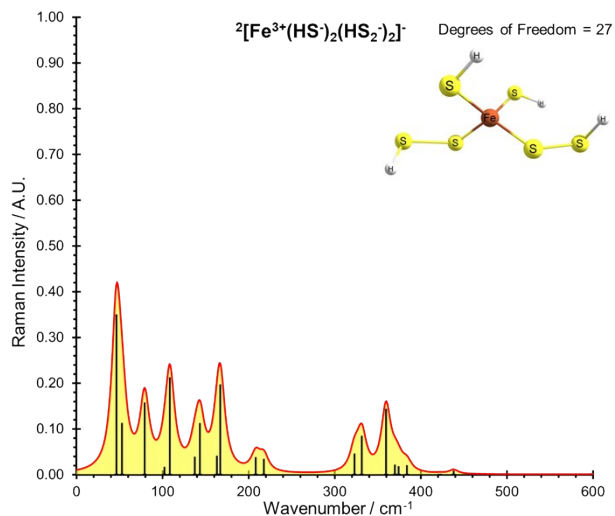


Figure S46. Calculated Raman spectrum of ${}^2[\text{Fe}^{3+}(\text{HS}^-)_2(\text{HS}_2^-)_2]^-$. The intensities for 27 degrees of freedom were scaled to the Raman band of ${}^6[\text{Fe}^{3+}(\text{HS}^-)_2(\text{HS}_2^-)_2]^-$ at 30 cm^{-1} .

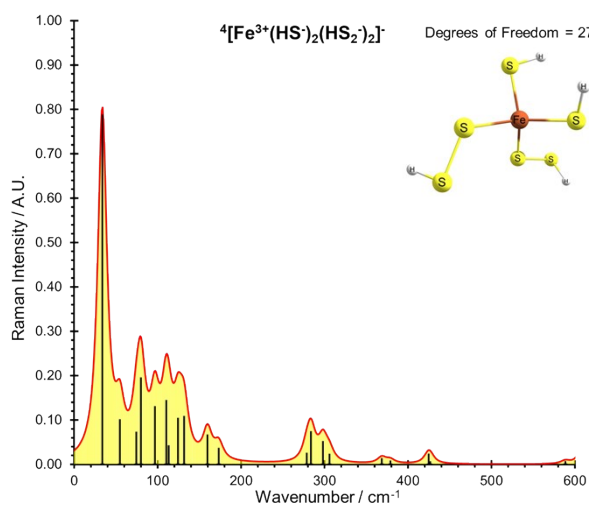


Figure S47. Calculated Raman spectrum of ${}^4[\text{Fe}^{3+}(\text{HS}^-)_2(\text{HS}_2^-)_2]^-$. The intensities for 27 degrees of freedom were scaled to the Raman band of ${}^6[\text{Fe}^{3+}(\text{HS}^-)_2(\text{HS}_2^-)_2]^-$ at 30 cm^{-1} .

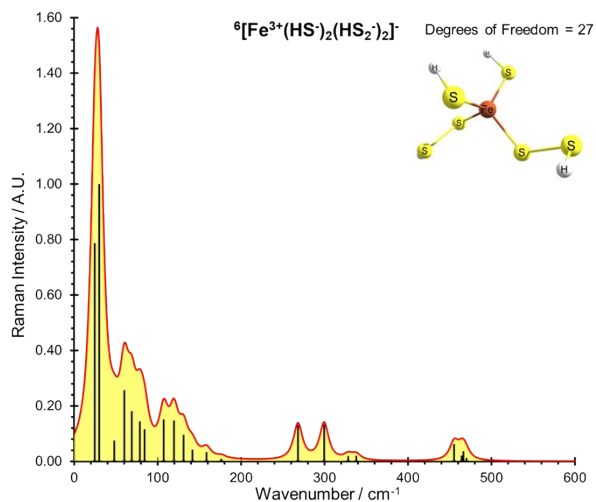


Figure S48. Calculated Raman spectrum of ${}^6[\text{Fe}^{3+}(\text{HS}^-)_2(\text{HS}_2^-)_2]^-$. The intensities for 27 degrees of freedom were scaled to the Raman band of at 30 cm^{-1} .

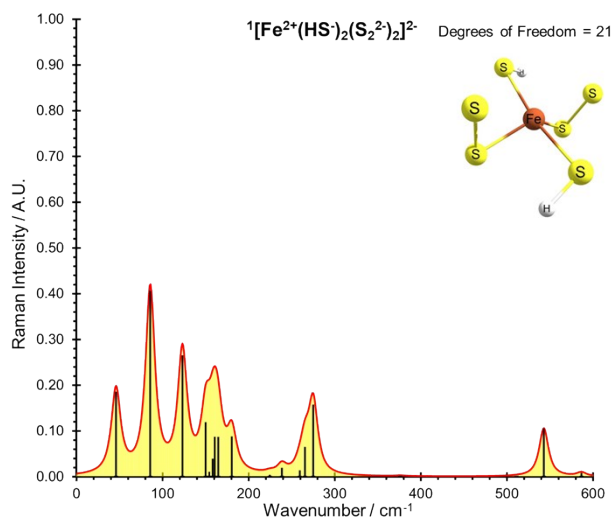


Figure S49. Calculated Raman spectrum of $^1[\text{Fe}^{2+}(\text{HS})_2(\text{S}_2^{2-})_2]^{2-}$. The intensities for 21 degrees of freedom were scaled to the Raman band of $^1[\text{Fe}^{2+}(\text{HS})_3(\text{S}_2^{2-})]^{3-}$ at 2216 cm^{-1} .

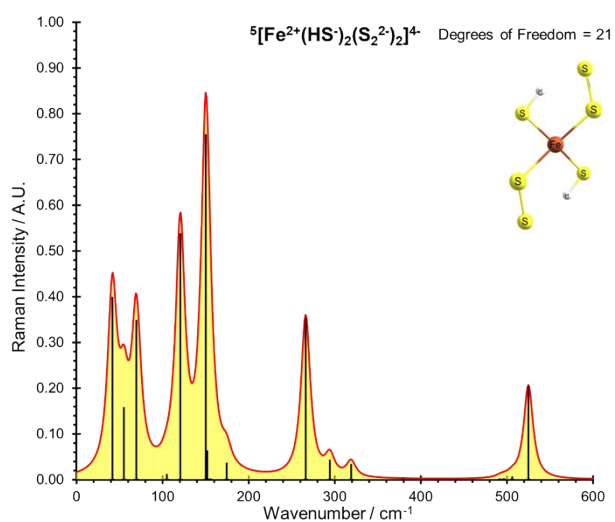


Figure S50. Calculated Raman spectrum of $^5[\text{Fe}^{2+}(\text{HS})_2(\text{S}_2^{2-})_2]^{4-}$. The intensities for 21 degrees of freedom were scaled to the Raman band of $^1[\text{Fe}^{2+}(\text{HS})_3(\text{S}_2^{2-})]^{3-}$ at 2216 cm^{-1} .

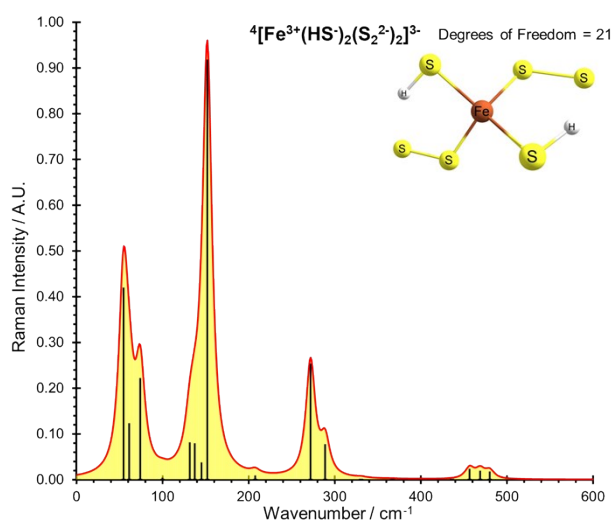


Figure S51. Calculated Raman spectrum of $^4[\text{Fe}^{3+}(\text{HS})_2(\text{S}_2^{2-})_2]^{3-}$. The intensities for 21 degrees of freedom were scaled to the Raman band of $^1[\text{Fe}^{2+}(\text{HS})_3(\text{S}_2^{2-})]^{3-}$ at 2216 cm^{-1} .

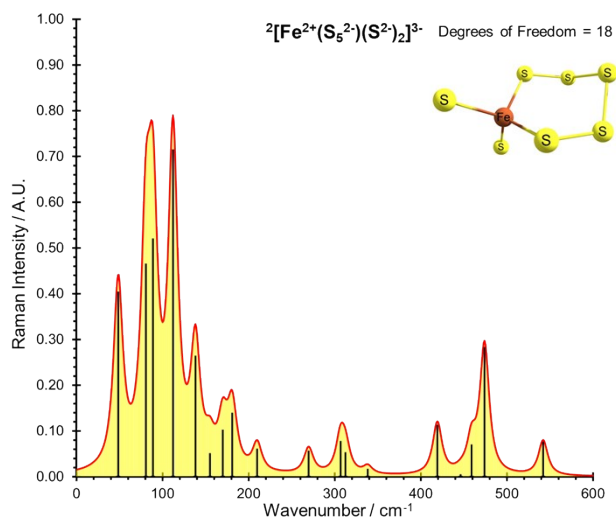


Figure S52. Calculated Raman spectrum of ${}^2[\text{Fe}^{2+}(\text{S}_5^{2-})(\text{S}^{2-})_2]^{3-}$. The intensities for 18 degrees of freedom were scaled to the Raman band of ${}^6[\text{Fe}^{3+}(\text{S}_5^{2-})(\text{S}^{2-})_2]^{3-}$ at 52 cm^{-1} .

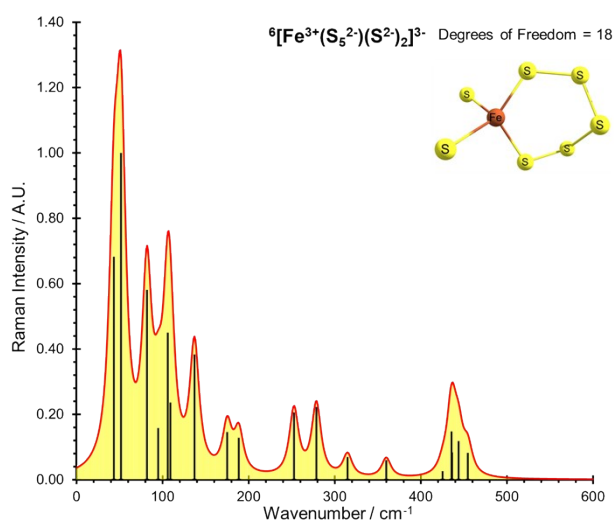


Figure S53. Calculated Raman spectrum of ${}^6[\text{Fe}^{3+}(\text{S}_5^{2-})(\text{S}^{2-})_2]^{3-}$. The intensities for 18 degrees of freedom were scaled to the Raman band of at 52 cm^{-1} .

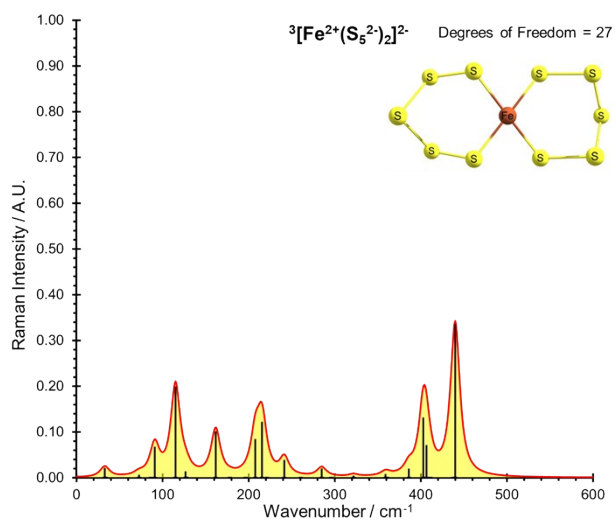


Figure S54. Calculated Raman spectrum of ${}^3[\text{Fe}^{2+}(\text{S}_5^{2-})_2]^{2-}$. The intensities for 27 degrees of freedom were scaled to the Raman band of ${}^6[\text{Fe}^{3+}(\text{HS}^-)_2(\text{HS}_2^-)_2]^-$ at 30 cm^{-1} .

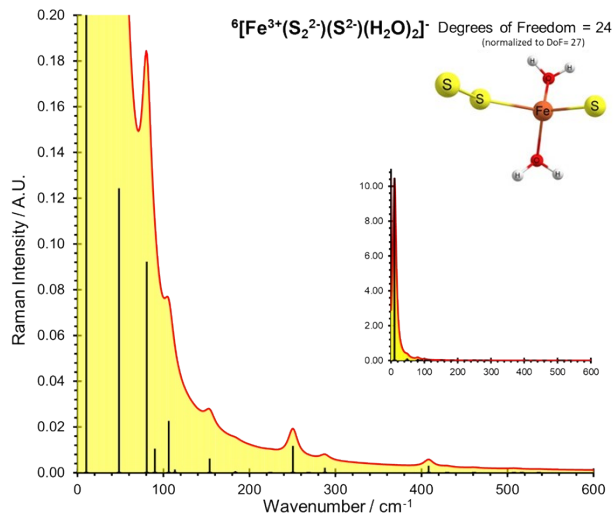


Figure S55. Calculated Raman spectrum of ${}^6[\text{Fe}^{3+}(\text{S}_2^{2-})(\text{S}^{2-})(\text{H}_2\text{O})_2]^-$. The intensities for 24 degrees of freedom were scaled to the Raman band of ${}^6[\text{Fe}^{3+}(\text{HS}^-)_2(\text{HS}_2^-)_2]$ at 30 cm^{-1} .

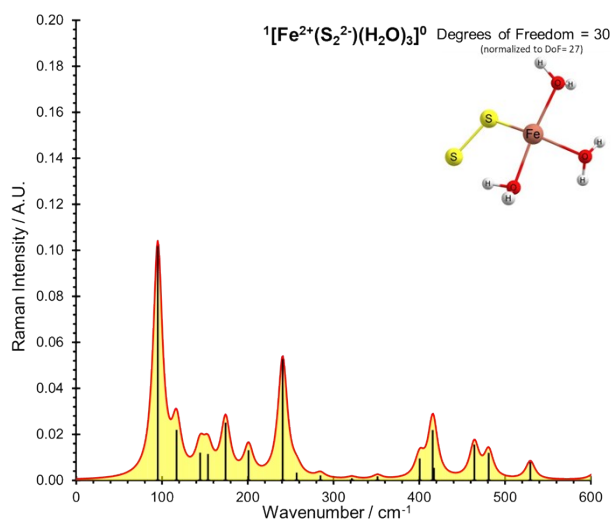


Figure S56. Calculated Raman spectrum of ${}^1[\text{Fe}^{2+}(\text{S}_2^{2-})(\text{H}_2\text{O})_3]^0$. The intensities for 30 degrees of freedom were scaled to the Raman band of ${}^6[\text{Fe}^{3+}(\text{HS}^-)_2(\text{HS}_2^-)_2]$ at 30 cm^{-1} .

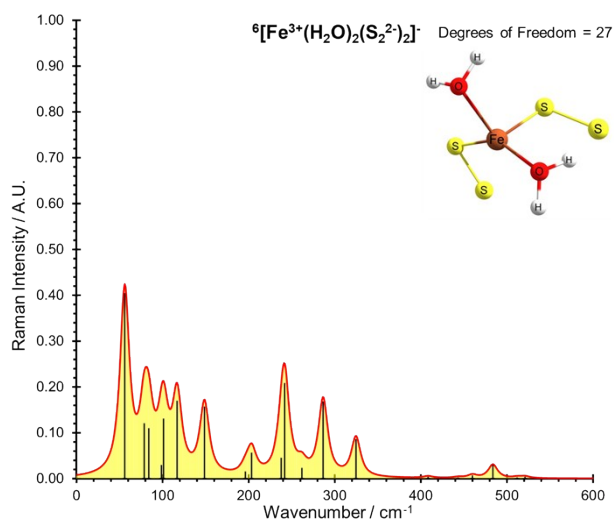


Figure S57. Calculated Raman spectrum of ${}^6[\text{Fe}^{3+}(\text{H}_2\text{O})_2(\text{S}_2^{2-})_2]^-$. The intensities for 27 degrees of freedom were scaled to the Raman band of ${}^6[\text{Fe}^{3+}(\text{HS}^-)_2(\text{HS}_2^-)_2]$ at 30 cm^{-1} .

6. Literature References:

- 1 R. S. Mulliken, *J. Chem. Phys.*, 1955, **23**, 1833–1840.
- 2 P. L. Polavarapu, *J. Phys. Chem.*, 1990, **94**, 8106–8112.
- 3 D. Michalska and R. Wysokiński, *Chemical Physics Letters*, 2005, **403**, 211–217.
4. Polavarapu, P. L. *Journal of Physical Chemistry*, 1990, **94**(21), 8106-8112.